

Final State Interactions in Near Threshold Meson Production from pp Collisions^{*†}

A. Sibirtsev, W. Cassing

Institut für Theoretische Physik, Universität Giessen
D-35392 Giessen, Germany

Abstract. We analyse the experimental data on near threshold π , η , ω , η' and K^+ production from pp collisions and show that all information gained so far is compatible with approximately constant production matrix elements when including the rescattering between the baryons in the final states. Different methods to include the final state interactions are discussed and their range of validity is indicated. We, furthermore, show that Dalitz plots for the proton-meson invariant mass spectra at different energies should be suited to distinguish between final state interactions and resonant production amplitudes.

1 Introduction

The strong interaction at low energies, i.e. elastic nucleon-nucleon scattering, is reasonably described by π , σ , η , ρ and ω -meson exchanges between the nucleons and the detailed experimental data on $NN \rightarrow NN$ reactions have provided information about the meson-nucleon-nucleon vertices, i.e. coupling constants and form factors. Above the pion production threshold the dominant inelasticity of the NN interactions is due to pion production. Already in 1960 Woodruff [1] proposed to extend the NN potential model in order to calculate $NN \rightarrow NN\pi$ reactions. Near the reaction threshold the contribution from Δ intermediate states is expected to be negligible and the S -wave pion production is governed by the πNN vertex. Thus pion production is suited to verify our knowledge about the πNN coupling constant.

A similar motivation also holds for near threshold η -meson production, when the S_{11} resonance replaces the Δ , and the η production cross section should provide some information about the ηNN vertex. Note that the status of the ηNN coupling constant is still an open problem [2, 3, 4] since within our present

^{*}Dedicated to Prof. A. Weiguny on occasion of his retirement

[†]Supported by FZ Jülich

knowledge $g_{\eta NN}$ might vary between 1 and 9 depending on the model adopted as well as the accuracy of the experimental data.

Near threshold ω , ϕ and η' -meson production in NN collisions should provide information about the relevant MNN couplings as well as on intermediate baryonic resonances that might be coupled strongly to these mesons; this is discussed as *hidden* resonance properties. Obviously the strangeness production in NN collisions involves an additional mechanism due to strange meson exchange (K, K^*) and sheds light on the kaon-hyperon-nucleon vertex.

We will base our analysis in this work on the combined efforts of many experimental groups that have taken data on near threshold meson production: These type of experiments for NN collisions were started at the Indiana University Cyclotron Facility with data on the $pp \rightarrow pp\pi^0$ reaction at excess energies $\epsilon = \sqrt{s} - 2m_N - m_\pi$ from $\simeq 1$ to $\simeq 30$ MeV [5, 6]. The data at $\epsilon \leq 1$ MeV were complemented by CELSIUS (Uppsala) [7]; recently also IUCF reported [8, 9] new cross sections on the $pp \rightarrow pn\pi^+$ reaction at $\epsilon < 20$ MeV. The near threshold η -meson production in pp collisions was studied at SATURNE by the collaborations SATURNE-II [10] and PINOT [11] and at CELSIUS [12]. These measurements cover the range $\simeq 1.5 \leq \epsilon \leq 100$ MeV. In 1998 CELSIUS reported also data [13] on the $pn \rightarrow pn\eta$ reaction at $16 \leq \epsilon \leq 100$ MeV. Additionally, the $pp \rightarrow pp\eta'$ reaction was studied at SATURNE by SPES-III [14] and at the COoler SYnchrotron (Jülich) by COSY-11 [15] at $\epsilon < 10$ MeV.

Furthermore, the $pp \rightarrow pp\omega$ reaction was measured at SATURNE by the DISTO Collaboration; they reported [16] data on ω -meson production from pp collisions at $\epsilon \simeq 320$ MeV and ϕ production at $\epsilon \simeq 82$ MeV. The data on the $pp \rightarrow pp\omega$ reaction at $\epsilon < 31$ MeV were measured by SPESIII and have been reported only very recently [17]. The $pp \rightarrow p\Lambda K^+$ reaction was measured by the COSY-11 [18] and the COSY-TOF [19] Collaborations; COSY-11 also has reported on the $pp \rightarrow p\Sigma^0 K^+$ reaction [20].

It should be noted that apart from the π^0 and η data the experimental results on near threshold meson production in NN collisions have become available only during the last years. This has initialized a lot of theoretical activity and inspired the most recent calculations within meson-exchange models. Here we present a systematical analysis of the data and provide the relation between the experimental observables and the production mechanism, respectively.

Our work is organized as follows: In Section 2 we will describe the threshold kinematics and discuss various approaches for the final state interactions (FSI). Section 3 is devoted to an analysis of the available data with the aim to extract average production matrix elements for the mesons measured so far. In Section 4 we will discuss the effect of FSI and resonance amplitudes on differential observables while Section 5 concludes this study with a summary.

2 Threshold kinematics and Final State Interactions

The threshold kinematics have several features that request specific conditions for the experimental measurements as well as the theoretical analysis. We note

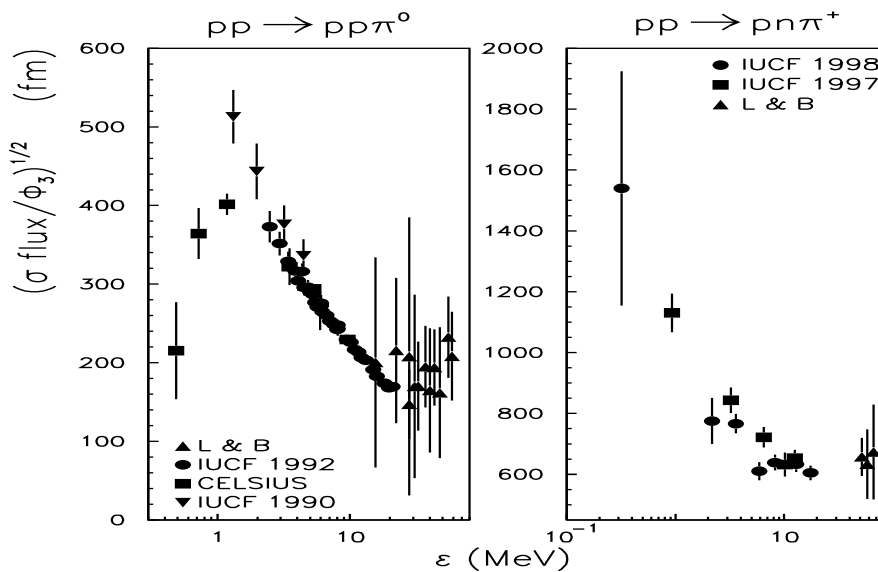


Figure 1. Experimental data on the $pp \rightarrow pp\pi^0$ [5, 6, 7, 23] and $pp \rightarrow pn\pi^+$ [8, 9, 23] reaction amplitude as a function of the excess energy ϵ .

that within nonrelativistic approaches the three-body phase space Φ_3 is proportional to ϵ^2 . Thus data on threshold meson production are frequently analyzed in terms of the *reduced cross section* σ/ϵ^2 . In [21] we have proposed to analyze the data in a more transparent way in terms of an average reaction amplitude (for fixed invariant energy \sqrt{s}) as

$$\begin{aligned}
 |M_R| &= 2^4 \pi^{3/2} \lambda^{1/4}(s, m_N^2, m_N^2) \sqrt{\sigma s} \\
 &\times \left[\int_{(m_b+m_c)^2}^{(\sqrt{s}-m_a)^2} \lambda^{1/2}(s, s_1, m_a^2) \lambda^{1/2}(s_1, m_b^2, m_c^2) \frac{ds_1}{s_1} \right]^{-1/2} \quad (1)
 \end{aligned}$$

with $\lambda(x, y, z) = (x - y - z)^2 - 4yz$ and m_a, m_b, m_c denoting the masses of the particles in the final state.

Furthermore, among the five variables characterizing the three-body final state, there are two of direct physical relevance: the invariant mass $\sqrt{s_1}$ of two final particles b and c and the 4-momentum squared t transferred from the initial nucleon to particle a . These variables allow to express the production amplitude in the meson-exchange mechanism. Note that $\sqrt{s_1}$ varies from $m_b + m_c$ up to $m_b + m_c + \epsilon$. Since the width of the known baryonic resonances is larger than 100 MeV, it is not possible - within a narrow ϵ range - to detect directly an intermediate baryonic resonance coupled to bc (meson + nucleon or hyperon) and to reconstruct experimentally the relevant production mechanism [4, 22]. Therefore complete measurements have to be performed at least

up to $\epsilon \simeq 100$ MeV.

Close to threshold both $\sqrt{s_1}$ and t vary only slightly and the production amplitude itself is expected to be almost constant. Fig. 1 shows the amplitudes for the $pp \rightarrow pp\pi^0$ and $pp \rightarrow pn\pi^+$ reactions extracted from the experimental data [5, 6, 7, 8, 9, 23] using Eq. (1). The amplitudes substantially depend on the excess energy ϵ but seem to approach a constant value for large excess energies. Such a deviation from a constant value has been predicted by Watson [24] and Migdal [25] due to the strong S -wave interaction between the final nucleons.

Indeed the Watson-Migdal theorem can be understood, for instance, in terms of the pp cross section shown in Fig.2a) as a function of the proton momentum q in the center-of-mass system. The cross section is enhanced at low q due to the 1S_0 partial wave [26] as shown by the solid line in Fig. 2a). Above about 400 MeV/c the elastic cross section approaches again a constant as indicated by the dashed line. It is thus expected that the production of mesons is enhanced when the protons emerge with a low relative momentum in the final state.

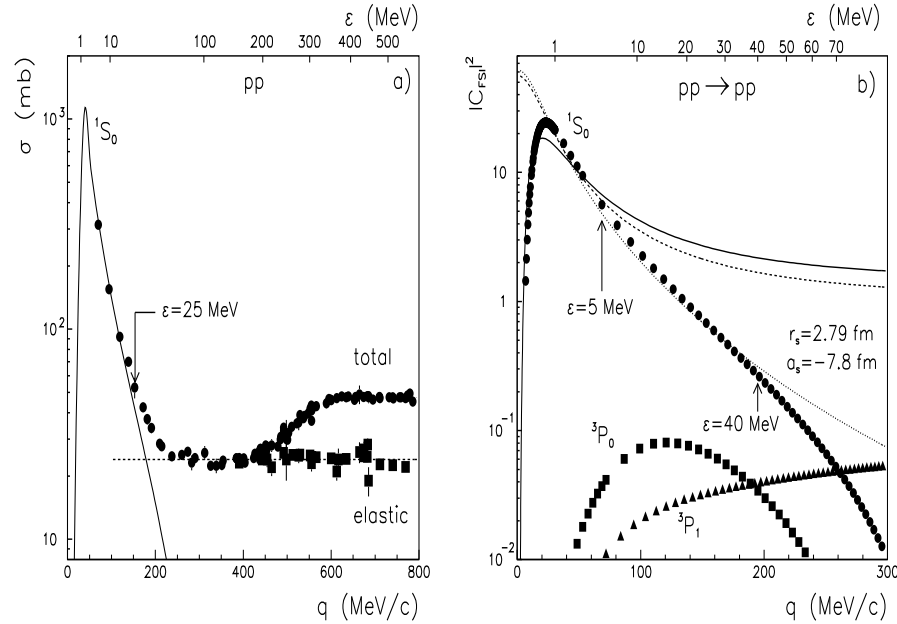


Figure 2. a) Total (circles) and elastic (squares) cross sections for the pp interaction as a function of the momentum in the pp cms. The data are from Ref. [23]. The solid line shows the contribution from the 1S_0 partial wave [26], while the dashed line indicates the large momentum limit. b) Correction factor due to final-state-interactions (FSI). The squared pp scattering amplitudes are shown for 1S_0 (circles), 3P_0 (squares) and 3P_1 (triangles) partial waves [27]. The dotted line shows the result from the effective range approximation, the dashed line shows the inverse squared Jost function without Coulomb correction, while the solid line includes a Coulomb correction. Further notations are explained in the text.

Note that in the $NN \rightarrow NNM$ reaction the momentum q varies from zero up to $\simeq \sqrt{m_N \epsilon}$. Obviously at large excess energies the contribution from FSI due to the strong S -wave to the total $pp \rightarrow pp\pi^0$ cross section seems to be not dominant, since one should integrate over the wide phase space. However, S -wave FSI can be detected by differential observables even at large ϵ as we will illustrate in the following. For $\epsilon \leq 25$ MeV the FSI between the protons is entirely due to the 1S_0 -wave. At higher energies the pp cross section deviates from the calculations with the 1S_0 phase shift as can be seen from Fig.2a) and is indicated by an arrow.

Now the deviation of the $NN \rightarrow NN\pi$ reaction amplitude shown in Fig.1 from a constant can be understood within the Watson-Migdal approximation. Moreover, the difference in the energy dependence of the $pp \rightarrow pp\pi^0$ and $pp \rightarrow pn\pi^+$ reaction amplitudes at $\epsilon \leq 1$ MeV is due to the Coulomb interaction between the final nucleons, which is absent in np scattering, but influences the final pp scattering for $\epsilon \leq 1$ MeV as can be seen from Fig.2b).

Taking the near threshold production amplitude M as a constant, it was proposed in Refs.[24, 25] to factorize the reaction amplitude M_R as

$$M_R = M \times C_{FSI}, \quad (2)$$

where C_{FSI} stands for the amplitude due to the interaction between the final particles. Strictly one should account for the three-body FSI, which itself is a rigorous problem. As was suggested by Gell-Mann and Watson [28] the near threshold $NN \rightarrow NN\pi$ reaction might be examined when considering the dominance of low energy NN scattering as compared to the S -wave πN interaction and taking C_{FSI} as the S -wave NN on-shell scattering amplitude T_s . Obviously, the produced particles are off-shell before rescattering due to FSI, which in principle involves an additional assumption about the off-shell correction to T_s .

Fig.2b) shows the squared 1S_0 , 3P_0 and 3P_1 pp scattering amplitudes calculated with the phase shifts from the Nijmegen partial wave analysis [27]. At low ϵ the S -wave amplitude dominates and for further implementation to $NN \rightarrow NNM$ calculations can be expressed within the effective range approximation as

$$T_s(q) = \left(-\frac{1}{a_s} + \frac{r_s q^2}{2} - iq \right)^{-1}, \quad (3)$$

where $a_s = -7.8$ fm and $r_s = 2.79$ fm [29] denote the scattering length and effective range, respectively. The effective range approximation is shown in Fig.2b) by the dotted line and is valid for excess energies ϵ from 1 up to 40 MeV.

Another way [30] to account for FSI is to express C_{FSI} as an inverse S -wave Jost function

$$C_{FSI}(q) = \frac{q + i\beta}{q - i\alpha}, \quad (4)$$

where the parameters α and β are related to the effective range parameters as

$$a_s = \frac{\alpha + \beta}{\alpha\beta}, \quad r_s = \frac{2}{\alpha + \beta}. \quad (5)$$

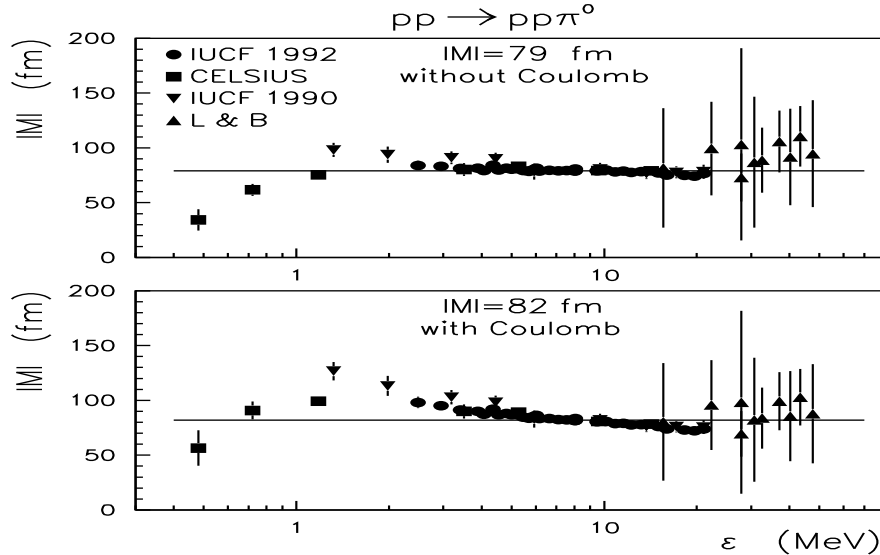


Figure 3. Experimental data [5, 6, 7, 23] on the average $pp \rightarrow pp\pi^0$ production amplitude as a function of the excess energy ϵ calculated without (upper part) and with Coulomb correction (lower part). The solid lines show the fit with a constant value for the production matrix element.

The squared inverse Jost function is shown by the dashed line in Fig.2b) and is close to the effective range approximation only for $\epsilon \leq 5$ MeV. Note that Eq.(4) approaches unity at large momenta q since the S -wave FSI does not contribute at large q , which is the proper boundary condition in terms of the factorization (2). Furthermore, to account for the Coulomb repulsion at $\epsilon \leq 1$ one can correct C_{FSI} in line with the Gamov factor (solid line in Fig. 2b).

Finally, when calculating the FSI within different approaches as the NN scattering amplitude itself or with the Jost function or an effective range approximation including Coulomb corrections we find no severe differences up to excess energies of $\simeq 5$ MeV. Furthermore, since the S -wave dominates the NN scattering up to $\epsilon \simeq 25$ MeV, the Jost function is an appropriate way to account for FSI corrections because it approaches unity at large ϵ in line with the factorization ansatz. The disadvantage of the method is due to the implementation of the on-shell $NN \rightarrow NN$ amplitude. However, off-shell corrections will introduce new parameters to the calculations that later on should be controlled by data.

3 Evaluation of the production amplitude from the data

Now we adopt the on-shell approach and use the Jost function in order to account for the FSI correction. Moreover, we perform the data analysis with and without Coulomb correction to demonstrate the systematic uncertainties. To calculate the production amplitude $|M|$ we substitute the function $C_{FSI}(q)$

in the integral of Eq.(1).

Fig.3 shows the average $pp \rightarrow pp\pi^0$ production amplitude as a function of the excess energy ϵ . In this representation the data are almost energy independent and approach a constant value. For $\epsilon < 1$ MeV two data points from Ref.[7] substantially deviate from the constant for calculations without the pp Coulomb repulsion, but become closer to a constant value after Coulomb correction. However, to shed light on the Coulomb effect one needs more data at $\epsilon < 1$ MeV. We also notice that the 1992 IUCF data [6] are better described by a constant amplitude $|M|$ as compared to the 1990 IUCF data [5]. Our analysis with Coulomb correction gives $|M| \approx 82$ fm for the $pp \rightarrow pp\pi^0$ reaction while we get $|M| \approx 79$ fm without this correction which indicates the systematic uncertainty of our analysis.

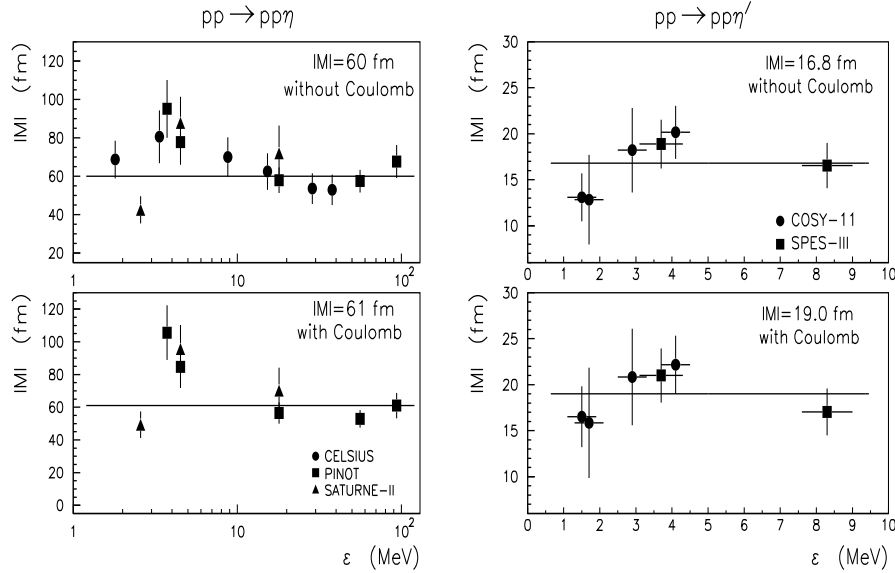


Figure 4. Experimental data on the average $pp \rightarrow pp\eta$ [10, 11, 12] and $pp \rightarrow pp\eta'$ [14, 15] production amplitudes calculated with and without Coulomb repulsion. The solid lines show the fit with a constant value for the production matrix element.

In a similar way we evaluate the average production amplitude from the total cross sections for the $pp \rightarrow pp\eta$ [10, 11, 12], $pp \rightarrow pp\omega$ [17] and $pp \rightarrow pp\eta'$ [14, 15] reactions and show the result in Figs.4,5. The results for the $pp \rightarrow pp\omega$ reaction are shown for a fixed ω -meson pole mass (squares) and for the calculation with a Breit-Wigner ω spectral function (circles), which is explicitly given as

$$|M_R| = 2^{9/2} \pi^2 \lambda^{1/4}(s, m_N^2, m_N^2) \sqrt{\sigma s} \left[\int_{m_\pi}^{\sqrt{s}-2m_N} \frac{\Gamma dx}{(x - m_\omega)^2 + \Gamma^2/4} \right]$$

$$\times \int_{4m_N^2}^{(\sqrt{s-x})^2} \lambda^{1/2}(s, s_1, x^2) \lambda^{1/2}(s_1, m_N^2, m_N^2) \left| C_{eff}(0.5\sqrt{s_1 - 4m_N^2}) \right|^2 \frac{ds_1}{s_1} \Big]^{-1/2} \quad (6)$$

with the vacuum ω -meson width $\Gamma=8.41$ MeV.

Again the deviation of the matrix element $|M|$ from a constant seems to be small for η , ω and η' production in pp collisions. The data are only available for $\epsilon > 1$ MeV and thus we can not observe the effect of the Coulomb pp final state repulsion. The calculations with and without Coulomb correction provide almost the same results for the production amplitudes, i.e. $|M| \approx 61$ fm for the η , $|M| \approx 33$ fm for the ω , and $|M| \approx 19.0$ fm for the η' -meson. Note that in case of the ω meson it is essential to account for the finite width of the spectral function close to threshold.

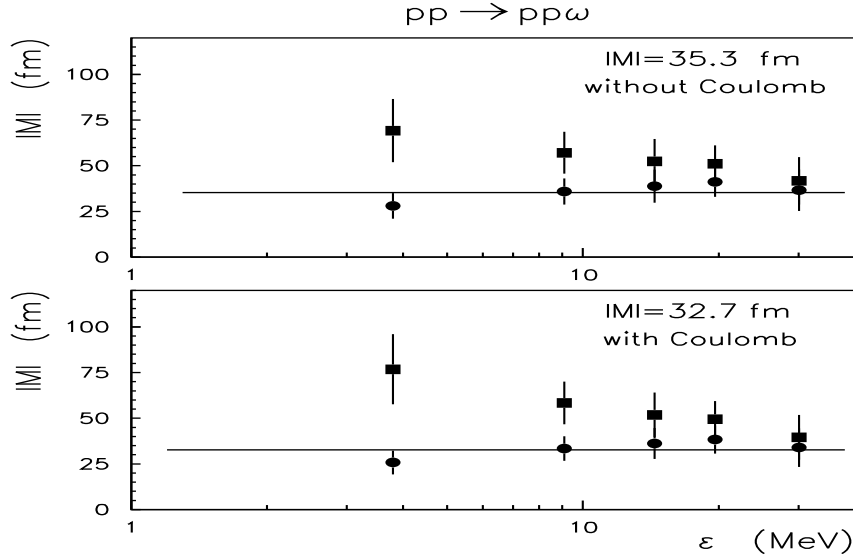


Figure 5. Experimental data on the average $pp \rightarrow pp\omega$ [17] production amplitudes calculated with and without Coulomb repulsion, for fixed ω mass (squares) and for the finite spectral function of the ω -meson with a width of 8.41 MeV (circles). The solid lines show the fit with a constant value for the production matrix element.

Recently IUCF published data on the $pp \rightarrow pn\pi^+$ reaction [8, 9] and CELSIUS reported $pn \rightarrow pn\eta$ [13] total cross sections. Both reactions are crucial for the verification of our approach, since the final np system does not suffer Coulomb repulsion as in case of the meson production data at $\epsilon \leq 1$ MeV. Fig.6 shows the $pp \rightarrow pn\pi^+$ and $pn \rightarrow pn\eta$ production amplitude extracted by Eq.1 with inclusion of the np FSI. Indeed, the two experimental points available at $\epsilon \leq 1$ MeV as well as the data for the $pp \rightarrow pn\pi^+$ cross section at higher excess energies are reproduced by a constant value of $|M| \approx 234$ fm. Fig.6 illus-

trates that the data for the $pn \rightarrow pn\eta$ reaction can be reasonably described by $|M| \approx 157$ fm.

Finally, the simple approach outlined above allows to evaluate the average production amplitudes from the total cross sections for $NN \rightarrow NN M$ reactions and enables one to subtract the FSI due to NN rescattering. The systematical analysis of the available experimental data on π^0 , π^+ , η and η' -meson production confirms the validity of the method proposed. Furthermore, the results illustrate a sensitivity to the difference between the pp and pn interactions in the final state and can be tested by data at excess energies below 1 MeV. Since the effective range parameters are the essential ingredients for our calculations, the method should be limited to $\epsilon \leq 40$ MeV (see Fig.2). However, at $\epsilon \geq 40$ MeV the NN scattering amplitude is almost energy independent and approaches a constant value, which might provide an explanation for the observation that the method seems to work even at higher energies.

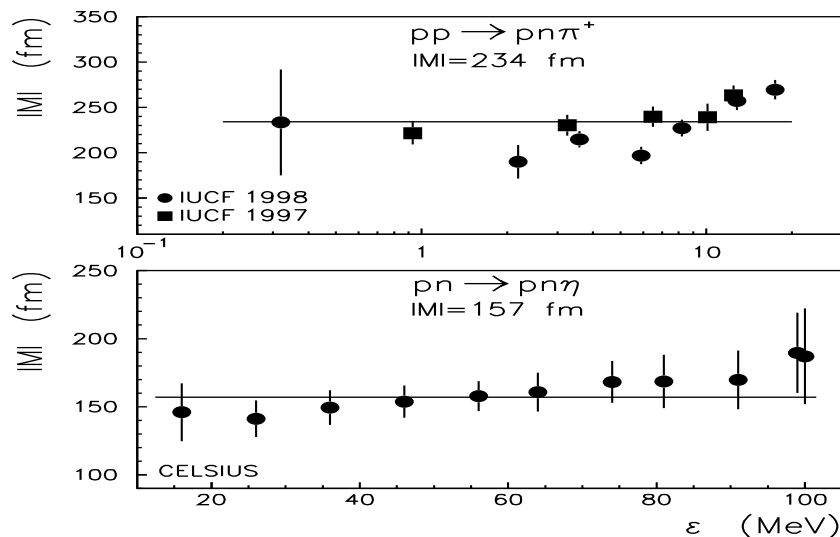


Figure 6. The data on the $pp \rightarrow pn\pi^+$ [8, 9] and $pn \rightarrow pn\eta$ [13] production amplitudes.

Indeed, the results for the $pp \rightarrow pp\eta$ and $pn \rightarrow pn\eta$ reactions indicate an almost constant value of $|M|$ up to $\epsilon \simeq 100$ MeV. This finding is in line with the meson exchange model for η -meson production due to the $S_{11}(1535)$ intermediate baryonic resonance excitation which provides the dominant S -wave production amplitude. A different situation holds for the $NN \rightarrow NN\pi$ reaction because at large ϵ the meson exchange model involves the $\Delta(1232)$ resonance and a strong contribution to the production amplitude due to the P -wave. Therefore, our approach can not be valid for π -meson production at large ϵ .

Recently the $pp \rightarrow pAK^+$ reaction was measured at COSY [18, 19]. The data indicate a strong deviation from the calculations with the one boson exchange

model [4, 31] at low ϵ due to the FSI between the proton and Λ -hyperon [21]. We have evaluated the $pp \rightarrow p\Lambda K^+$ production amplitude with the singlet 1S_0 and triplet 3S_1 effective range parameters for Λp scattering from Ref.[29] (model a) and show the result in Fig.7. Again the data can be reasonably reproduced with $|M| \approx 43$ fm over the available range of the excess energy.

We mention that the parameters for the YN interactions cannot be fitted uniquely to the available YN scattering data since experimental results are very scarce and have large statistical and systematical uncertainties. In turn the $pp \rightarrow NYK$ reaction might serve as an additional source for the examination of the hyperon-nucleon interaction at low relative momenta.

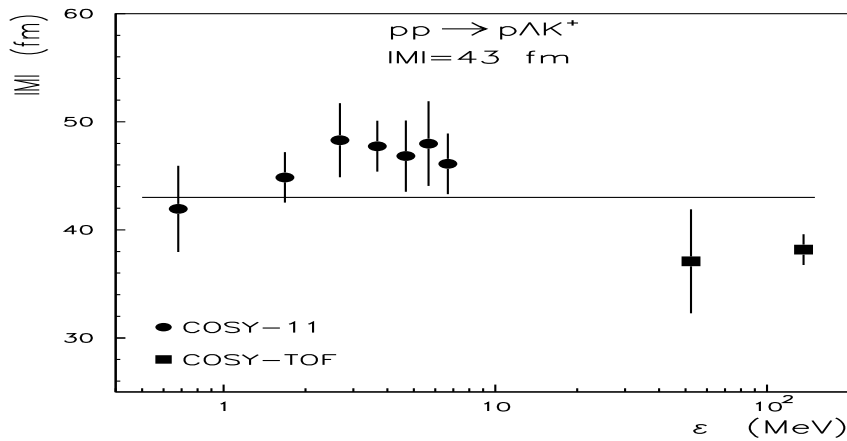


Figure 7. Experimental data on the average $pp \rightarrow p\Lambda K^+$ [18, 19] production amplitudes. The solid lines show a fit with $|M|=43$ fm.

Furthermore, to analyze the $pp \rightarrow p\Sigma^0 K^+$ data [20] one needs accurate coupled channel calculations that include the $\Sigma^0 p \leftrightarrow \Lambda p$ transition as well as $\Sigma^0 p \rightarrow \Sigma^0 p$ effective range parameters, which are not available by now [32].

The Tables 3.1 and 3.2 show the averaged production amplitudes evaluated from the data for the reactions discussed above. We separately show the results from different experiments, which are in reasonable agreement with each other. For the $pp \rightarrow pp\pi^0$, $pp \rightarrow pp\eta$ and $pp \rightarrow pp\eta'$ reactions the results are shown with and without Coulomb correction to the pp FSI.

Finally, due to the FSI the total production cross section is strongly enhanced at low excess energies as illustrated by Fig.8 which shows the $pp \rightarrow pp\eta'$ cross section as a function of ϵ calculated in the pion exchange model [33]. The dotted line indicates the calculations without the FSI and substantially underestimates the experimental results [14, 15]. Now taking into account the s -wave interaction between the final protons we reasonably reproduce the available data. Note that the Coulomb corrections influence the results for $\epsilon \leq 10$ MeV.

Our calculations illustrate that FSI change the energy dependence of the $pp \rightarrow pp\eta'$ cross section as compared to the pure phase space ϵ^2 . Note that the

Table 3.1. The $pp \rightarrow pp\pi^0$, $pp \rightarrow pp\eta$, $pp \rightarrow pp\omega$ and $pp \rightarrow pp\eta'$ production amplitudes $|M|$ evaluated from the data with and without the Coulomb corrections.

Reference	without Coulomb		with Coulomb	
	$ M $ (fm)	χ^2	$ M $ (fm)	χ^2
$pp \rightarrow pp\pi^0$				
IUCF [5]	84.2	1.8	88	6.5
IUCF [6]	79.0	0.8	81.7	4.8
CELSIUS [7]	79.9	7.8	83.1	13.4
$pp \rightarrow pp\eta$				
SATURNE-II [10]	55	5.1	62	3.9
PINOT [11]	63	1.9	60	3.3
CELSIUS [12]	61	1.1	61	2.5
$pp \rightarrow pp\omega$				
SPES-III [17]	35.3	0.5	32.7	0.5
$pp \rightarrow pp\eta'$				
SPES-III [14]	17.6	0.4	18.7	1.0
COSY-11 [15]	16.1	1.3	19.3	0.6

Table 3.2. The $pp \rightarrow pn\pi^+$, $pn \rightarrow pn\eta$ and $pp \rightarrow p\Lambda K^+$ production amplitudes $|M|$.

Reference	$ M $ (fm)	χ^2
$pp \rightarrow pn\pi^+$		
IUCF [8]	240	1.8
IUCF [9]	228	6.8
$pn \rightarrow pn\eta$		
CELSIUS [13]	157	0.5
$pp \rightarrow p\Lambda K^+$		
TOF [19]	38	0.05
COSY-11 [18]	46.3	0.41

results without FSI (dotted line in Fig.8) might, in principle, be renormalized in order to fit the data [14, 15] for $\epsilon \leq 10$ MeV, however, the increase with ϵ would be much faster. This indicates that in order to determine the FSI experimentally one needs data on the total production cross section from threshold up to about 100 MeV in excess energy.

4 FSI and differential observables

Obviously the FSI effect differential observables in a more pronounced way than the total production cross section. Fig.2 shows that the s -wave dominates the low energy proton-proton scattering and accordingly enhances the low energy

part of the pp invariant mass distribution. Thus, due to energy conservation, the high energy part of the final meson-baryon invariant mass distribution is also enhanced. Let us illustrate this for the $pp \rightarrow pp\eta'$ reaction.

Since there are no data on baryonic resonances that couple to the η' -meson, our calculations [33] for the $pp \rightarrow pp\eta'$ reaction have been carried out within the pion exchange model without explicitly introducing intermediate baryonic resonances. Thus any deviation of the calculated differential observables for the $pp \rightarrow pp\eta'$ reaction at low ϵ from phase space only stems from the s -wave FSI between the protons.

Fig.9a) shows the Dalitz plot for the $pp \rightarrow pp\eta'$ reaction at $\epsilon=10$ MeV. Indeed the distribution is enhanced at low pp and large $p\eta'$ masses. Figs. 9b,c), furthermore, show the c.m.s. momentum spectra of the η' -mesons and protons produced in the $pp \rightarrow pp\eta'$ reaction at $\epsilon=10$ MeV. The solid histograms display our calculations within the pion exchange model [33] including the FSI. The dashed histograms are the results without FSI but corrected by a factor 8.12 due to the difference in the total cross section calculated with and without FSI (see Fig.8). The impact of the FSI is obvious and can be easily detected in the η' -spectra. It is important to note that the distortion of the phase space distribution due to the FSI should be properly taken into account when extrapolating experimental data in a limited acceptance to 4π .

Moreover, the FSI produce some resonance structure in the meson-baryon invariant mass distribution as shown in Fig.10a,b) for the $pp \rightarrow pp\eta'$ reaction at $\epsilon=10$ MeV and $\epsilon=100$ MeV. Here the solid histograms are our calculations with FSI while the dotted histograms show the results calculated without FSI which

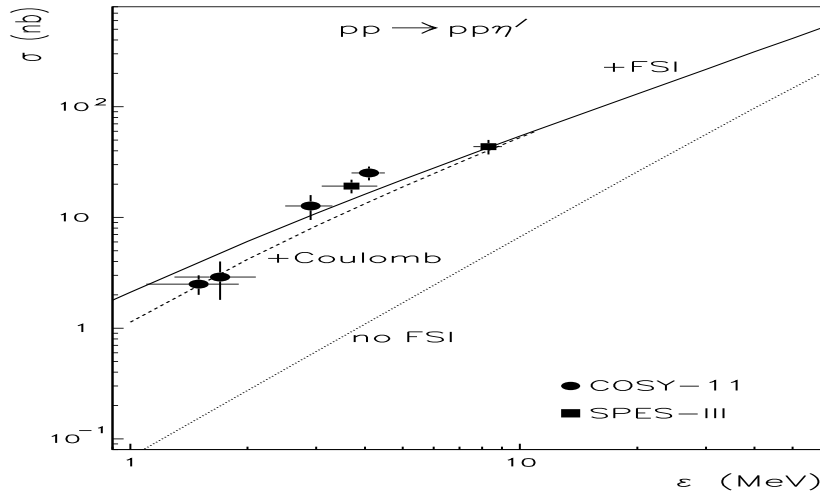


Figure 8. The total cross section for the $pp \rightarrow pp\eta'$ reaction. The experimental data are from Ref.[14, 15] while the lines show the calculations with the pion exchange model [33] without FSI between the protons (dotted), with FSI (solid) and with Coulomb corrections to FSI (dashed).

are similar to the pure phase-space distributions. The dashed histograms in Figs. 10a,b) are the calculations without FSI but renormalized to the same total production cross section. Recall that we do not include intermediate baryonic resonances in our model [33] and that the *pseudo* resonance structure in the $p\eta'$ mass spectra stems from the FSI.

Experimentally this effect can be detected when analyzing the compatibility ratio, i.e. the ratio of the measured invariant mass spectra to the phase space distribution that is normalized to the experimental total cross section. The calculated compatibility ratio for the $pp \rightarrow pp\eta'$ reaction at $\epsilon=10$ MeV and 100 MeV is shown in Figs. 10c,d) and visibly deviates from unity. Recall that in the absence of FSI as well as other effects, e.g. an excitation of a baryonic resonance in the meson-baryon system or the appearance of higher partial waves in the production amplitude (which might happen at large ϵ), the compatibility ratio should approach unity. On the other hand, to detect the distortion of the compatibility ratio one needs sufficiently large statistical accuracy as can be seen from Figs. 10c,d).

In order demonstrate how an intermediate resonance shows up in the invariant mass spectra we analyze the $pp \rightarrow pp\eta$ reaction calculating the production amplitude due to the excitation of the $S_{11}(1535)$ resonance. Fig.11 shows the resulting $p\eta$ invariant mass spectra for $\epsilon=10, 100, 150$ and 200 MeV. The solid histograms are our calculations with the $S_{11}(1535)$ and FSI, while the dotted histograms indicate the results without FSI between the protons. The dotted

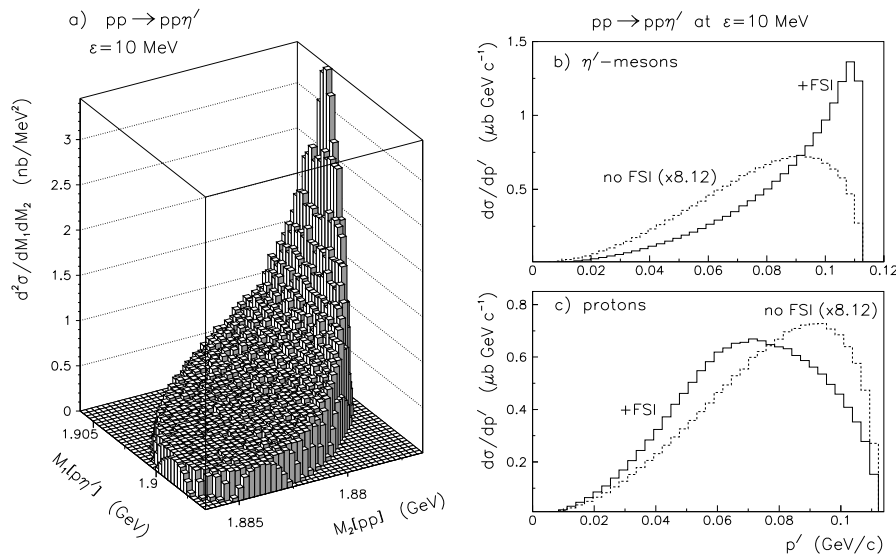


Figure 9. The differential observables for the $pp \rightarrow pp\eta'$ reaction at $\epsilon=10$ MeV. a). The Dalitz plot calculated within the pion exchange model and with FSI. b-c). The momentum spectra of the η' -mesons and protons in the center of mass system calculated with (solid) and without FSI (dashed histograms). The calculations without FSI have been renormalised to the same total cross section.

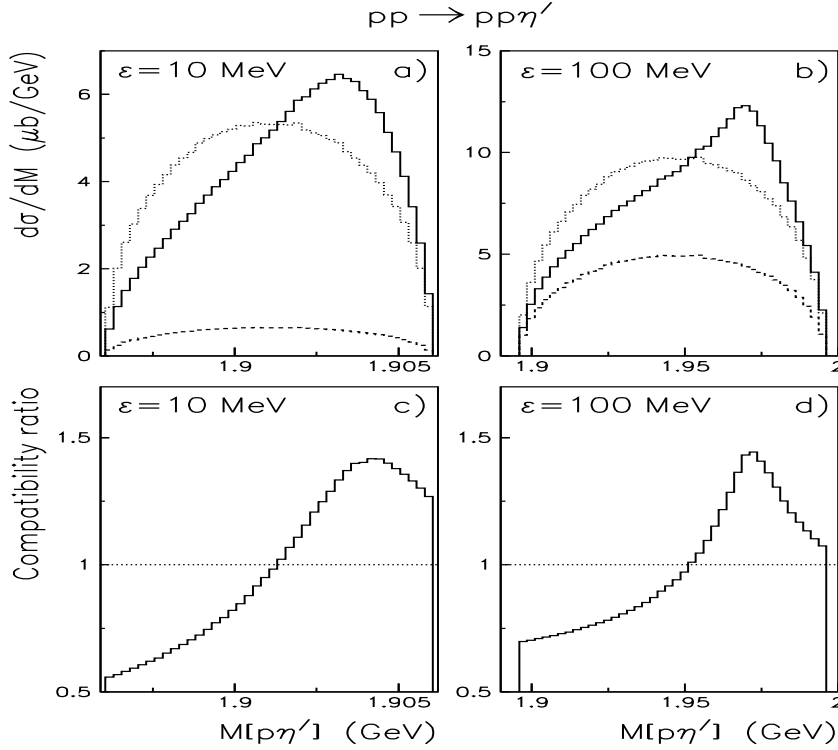


Figure 10. The $p\eta'$ invariant mass spectra (a,b) and the compatibility ratio (c,d) calculated for the $pp \rightarrow pp\eta'$ reaction at $\epsilon=10$ MeV and 100 MeV. The histograms in a),b) show the results with FSI (solid), without FSI (dotted) and without FSI but renormalized to the same cross section(dashed).

lines in Fig.11 show the phase-space distribution normalized to the calculated total cross section.

As discussed above, the S_{11} structure cannot be detected at $\epsilon \leq 100$ MeV since the width of the baryonic resonance is larger than the range of the $p\eta$ invariant mass. Furthermore, the shape of the spectra calculated with a S_{11} intermediate resonance and without FSI are similar to the spectra in line with phase space at $\epsilon \leq 100$ MeV. The deviation of the $p\eta$ mass spectra at $\epsilon=10$ and 100 MeV from phase space (dotted lines) is entirely due to FSI.

The S_{11} structure can be detected at $\epsilon=150$ and 200 MeV where the $p\eta$ mass spectra calculated even without FSI (dashed histograms) differ already from pure phase space. Note, however, that FSI substantially distort the spectra and consequently we find two structures in the $p\eta$ invariant mass distributions. The enhancement around $M_{p\eta}$ is due to the S_{11} resonance while the structure close to the kinematical limit of the $p\eta$ mass spectra stems from the FSI. Again the compatibility ratio might serve as a promising tool to detect the reaction mechanism.

Recently CELSIUS reported [34] the η -meson c.m.s. energy spectrum mea-

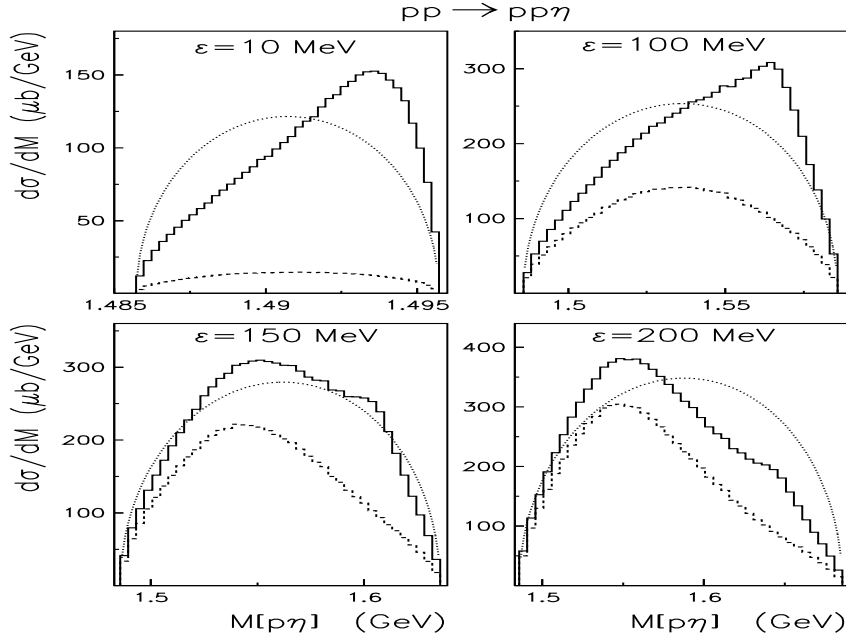


Figure 11. The $p\eta$ invariant mass spectra for the $pp \rightarrow pp\eta$ reaction at $\epsilon=10$ MeV, 100, 150 and 200 MeV. The solid histograms are calculations with an excitation of $S_{11}(1535)$ and FSI, while the dashed histograms show the results with $S_{11}(1535)$ but without FSI. The dotted lines indicate the normalized phase-space distributions.

sured in the $pp \rightarrow pp\eta$ reaction at $\epsilon=16$ MeV which is shown in Fig.12 together with our calculations. The solid histogram in Fig.12 shows the result with FSI that reasonably reproduces the data; the dashed histogram indicates the result without FSI and substantially differs from the experimental spectrum both in the absolute height and in shape. This comparison, furthermore, demonstrates the validity of our approach which is of sufficient simple form to be used in all data analysis for near threshold reactions.

5 Summary

In this work we have proposed a simple method to analyze or calculate cross sections on near threshold meson production in pp collisions by dividing out kinematical factors and accounting for final-state-interactions (FSI) between the nucleons including approximately also Coulomb corrections. Our analysis of the various models for FSI has shown that the inverse Jost-function method has the largest range of applicability, possesses the correct boundary condition for large excess energies and, furthermore, only involves the effective range parameters a_s and r_s that can be taken from a fit to the respective s -wave scattering amplitude.

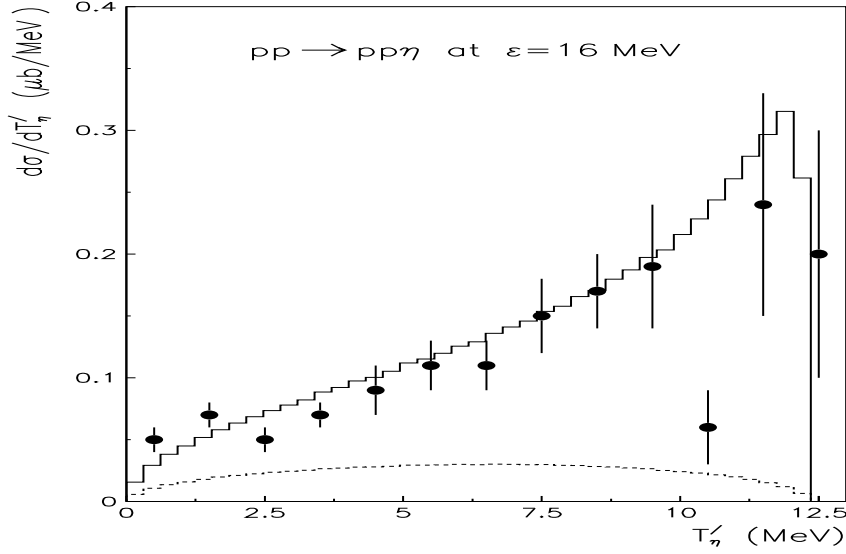


Figure 12. The η -meson energy spectrum in the center-of-mass system measured for the $pp \rightarrow pp\eta$ reaction at $\epsilon=16$ MeV. The full dots show the experimental results from Ref.[34] while the solid histogram is our calculation with FSI, the dashed histogram without FSI.

Within this model we have analyzed the available data on π , η , ω , η' and $K^+\Lambda$ production and found that all data are approximately compatible with constant production matrix elements. This information now in turn can be used to calculate reaction channels with different final states of the baryons if their FSI is known. On the other hand, the constant matrix element hypothesis allows to *measure* the FSI of baryons that are not available for scattering experiments. Note, however, that precise data up to excess energies of ≈ 100 MeV will be necessary.

Furthermore, we have shown that a differential data analysis in terms of Dalitz-plots allows to distinguish effects from final state interactions and resonance amplitudes if data are available in a sufficiently wide energy range comparable at least to the width of the resonance amplitude.

References

1. Woodruff, A.E.: Phys. Rev **117**, 1113 (1960)
2. Tiator, L., Benhold, C., Kamalov, S.S.: Nucl. Phys. **A580**, 455 (1994)
3. Feuster, T., Mosel, U.: Phys. Rev. **C59**, 460 (1999)
4. Sibirtsev, A., Tsushima, K., Cassing, W., Thomas, A.: Nucl. Phys. **A646**, 423 (1999)

5. Meyer, H.O., et al.: Phys. Rev. Lett. **65**, 2846 (1990)
6. Meyer, H.O., et al.: Nucl. Phys. **A539**, 633 (1992)
7. Bondar, A., et al.: Phys. Lett. **B356**, 8 (1995)
8. Hardie, J.G., et al.: Phys. Rev. **C56**, 20 (1997)
9. Flammang, R.W., et al.: Phys. Rev. **C58**, 916 (1998)
10. Bergdolt, A.M., et al.: Phys. Rev. **D48**, 2969 (1993)
11. Chiavassa, E., et al.: Phys. Lett. **B322**, 270 (1994)
12. Calén, H., et al.: Phys. Lett. **B366**, 39 (1996)
13. Calén, H., et al.: Phys. Rev. **B58**, 2667 (1998)
14. Hibou, F., et al.: Phys. Lett. **B438**, 41 (1998)
15. Moscal, P., et al.: Phys. Rev. Lett. **80**, 3202 (1998)
16. Balestra, F., et al.: Phys. Rev. Lett. **81**, 4572 (1998)
17. Hibou, F., et al.: nucl-ex/9903003.
18. Balewski, J.T., et al.: Phys. Lett. **B420**, 211 (1998); Eur. Phys. J. **A2**, 99 (1998)
19. Bilger, B., et al.: Phys. Lett. **B420**, 217 (1998)
20. Sewerin, S. et al.: nucl-ex/9811004
21. Sibirtsev, A., Cassing W.: nucl-th/9802025; Sibirtsev, A.: Acta Phys. Polon. **B29**, 3123 (1998)
22. Sibirtsev, A., Tsushima, K., Thomas, A.W.: Phys. Lett. **B421**, 59 (1998)
23. Landolt-Börnstein, New Series **I/12**, ed. Schopper, H., Springer 1998
24. Watson, K.M., Phys. Rev. **88**, 1163 (1952)
25. Migdal, A.B., JETP **1**, 2 (1955)
26. Arndt, R.A., Oh, C.H., Strakovsky, I.I., Workman, R.L., Dohrmann, F.: Phys. Rev. **C 56**, 3005 (1997)
27. Stoks, V.G.J., Klomp, R.A.M., Rentmeester, M.C.M., de Swart, J.J., Phys. Rev. **C 48**, 792 (1993)
28. Gell-Mann, M., Watson, K.M.: Ann. Rev. Nucl. Sci. **4**, 219 (1954)
29. Stoks, V.G.J., Rijken, Th.A.: nucl-th/9901028
30. Taylor, J.R., *Scattering Theory* (Wiley, New York, 1972)

31. Sibirtsev, A: Phys. Lett. **B 359**, 29 (1995); Tsushima, K., Sibirtsev, A., Thomas, A.W.: Phys. Lett. **B 390**, 29 (1997)
32. Stoks, V.G.J.: private communication
33. Sibirtsev, A, Cassing, W.: Eur. Phys. J. **A 2**, 333 (1998)
34. Calén, H., et al.: nucl-ex/9811003